

and subsequent adiabatic expansion from 2 to 3, (iii) establishment of thermal contact with the entropy sink to effect isothermal compression from 3 to 4 at temperature  $T_c$ , and (iv) breaking of thermal contact and continuance of adiabatic compression from 4 to 1.

We define the efficiency of the photo-Carnot engine as  $\eta = (Q_{in} - Q_{out})/Q_{in} = (T_h S_{12} + T_c S_{43})/T_h S_{12}$ . In the high-temperature ( $kT \gg \hbar\Omega$ ) and small expansion ( $\Delta\Omega = \Omega_1 - \Omega_2 \ll \Omega$ ) limits,  $S_{12} = S_{43} = k\Delta\Omega/\Omega$ .

Engine efficiency, when fueled by regular thermal atoms, is then given by  $\eta = 1 + (T_c S_{34}/T_h S_{12}) = 1 - T_c/T_h$ . However, when the radiation working fluid is heated by phase-coherent atoms,  $T_h \rightarrow T_\phi$  and the Carnot efficiency is given by

$$\eta_\phi = \eta - \frac{T_c}{T_h} 3\bar{n} |\rho_{bc}| \cos\phi \quad (7)$$

where  $\varepsilon = 3|\rho_{bc}| \ll 1$ . Hence,  $\eta_\phi > \eta$  when, for example,  $\phi = \pi$ .

We see from Eq. 7 that when  $T_h = T_c$  and  $\eta_\phi = 3\bar{n} |\rho_{bc}|$ , the photon engine produces work from a single heat bath. The net work produced, when  $T_h = T_c$ , is

$$W_{net} = \eta_\phi T_c S_{12} \approx \frac{\bar{n}\theta_\mu \hbar\omega}{kT} kT_c \frac{\Delta\Omega}{\Omega} = \bar{n}\theta_\mu \frac{\Delta\Omega}{\Omega} \hbar\omega \quad (8)$$

where the ‘‘Rabi flopping’’ angle  $\theta_\mu$  is the (small) tipping angle defined below.

The atomic coherence can be generated, for example, by passage of the atoms through a microwave field (12), which may be approximated by a coherent state  $|\alpha_\mu\rangle$  that has a mean photon number  $N_\mu = |\alpha_\mu|^2$ . If the resonant atom-field coupling frequency is  $g_\mu$ , and the interaction time is  $\tau_\mu$ , then  $\rho_{bc} \approx \theta_\mu \exp(i\phi)\hbar\omega/3kT$ , where  $\theta_\mu = g_\mu \tau_\mu |\alpha_\mu|$  and we have taken the high-temperature limit  $\rho_{cc} - \rho_{bb} \approx \hbar\omega/3kT$ . We may then write  $3\bar{n} |\rho_{bc}| = \bar{n}\theta_\mu \hbar\omega/kT$ . Hence if we take reasonable values;  $\theta_\mu \approx 0.1$ ,  $\omega/\Omega \approx 0.1$ , and  $\bar{n} \approx 10^3$ , we find  $|\rho_{bc}| \approx 3 \times 10^{-6}$ . Hence, for  $|\rho_{bc}|$  of order  $10^{-5}$ , efficiencies  $\eta_\phi$  are of a few percent (10, 11) even though  $T_h = T_c$ .

Heating effects governed by  $\Delta$  are unimportant in determining the temperature of the field. The atomic density matrix after microwave preparation is given by Eq. 6, where  $\Delta \sim \theta_\mu^2 \hbar\omega/kT$  is higher order in  $\theta_\mu$ . Furthermore, the effects of  $\Delta$  cancel out as can be seen in Eq. 5 and if  $\rho_{bb}$  is replaced with  $P_b + \Delta$  and  $\rho_{cc}$  is replaced with  $P_c - \Delta$ . Hence, the physics is contained in  $\rho_{bc}$ .

We can estimate the microwave energy,  $W_\mu$ , necessary to produce coherence between  $b$  and  $c$ , given the preceding microscopic model of our QHE (10, 11). The important point is that we find  $W_\mu \approx 5W_{net}$ , i.e.,  $W_\mu > W_{net}$  in the present QHE.

The quantum thermodynamics of systems slightly out of equilibrium is an area of cur-

rent interest (22). In the particular form of nonequilibrium considered here, quantum coherence, the phase  $\phi$  is found to be a demonstrable control parameter that allows work to be extracted from a single bath. The total system entropy is constantly increasing, and the physics behind the second law is not violated. However, quantum coherence does allow certain features of engine operation beyond the classical limit.

References and Notes

1. For an in-depth treatment, see K. Annamalai and I. Puri, *Advanced Thermodynamic Engineering* (CRC Press, Boca Raton, FL, 2001).
2. M. O. Scully, M. S. Zubairy, *Quantum Optics* (Cambridge Press, London, 1997).
3. Reviews of LWI are to be found in (23–25). The present scheme is closest to the lasing without inversion model of (26).
4. For example (27, 28).
5. H. Linke et al., *Science* **286**, 2314 (1999).
6. Two classic papers on information erasure and related subjects are (29, 30).
7. M. Scully, *Phys. Rev. Lett.* **87**, 220601 (2001).
8. ———, *Phys. Rev. Lett.* **88**, 050602 (2002).
9. S. Lloyd, M. Scully, in preparation.
10. M. Scully, in *Quantum Limits to the Second Law*, D. Sheehan, Ed. (AIP Press, New York, 2002), pp. 83–91.
11. M. S. Zubairy, in *Quantum Limits to the Second Law*, D. Sheehan, Ed. (AIP Press, New York, 2002), pp. 92–97.
12. Y. Rostovtsev, Z. Sariyanni, M. Scully, in preparation.
13. N. Ramsey, *Phys. Rev.* **103**, 20 (1956).
14. H. Skovil, E. Schultz-Dubois, *Phys. Rev. Lett.* **2**, 262 (1959).
15. See, for example (31–33) and references therein.
16. C. Bender, D. Brody, and B. Keister, *Proc. R. Soc. London A* **458**, 1519 (2002).
17. T. Opatrny, M. Scully, *Fortschr. Phys.* **50**, 657 (2002).
18. M. H. Lee, *Am. J. Phys.* **69**, 874 (2001).
19. D. Meschede, H. Walther, G. Muller, *Phys. Rev. Lett.* **54**, 551 (1985). For discussion of cavity QED, see (34, 35). For the quantum theory of a micromaser, see (36). For the first demonstration of the microlaser, see (37).
20. M. Kim, F. Narducci, M. O. Scully, M. S. Zubairy, in *Spectroscopy of Systems with Spatially Confined Structures*, B. Di Bartolo, Ed. (Kluwer, Netherlands 2002).
21. A complication arises as the cavity resonant frequen-

cy continuously changes during the passage of atoms through the cavity: the atoms may go out of resonance. To preserve resonance, we needed to continuously change the level spacing of the atoms. This can be accomplished in several ways, but for the present purposes we will simply take such atomic fine tuning as a given. Further discussion will be given elsewhere.

22. See, for example, the conference proceedings on the subject referred to in (10, 11) and references therein.
23. O. Kocharovskaya, *Phys. Rep.* **219**, 175 (1992).
24. E. Arimondo, *Prog. Opt.* **35**, 257 (1996).
25. S. Harris, *Phys. Today* **50**, 36 (1997).
26. M. Scully, S.-Y. Zhu, A. Gavrielides, *Phys. Rev. Lett.* **62**, 2813 (1989).
27. H. S. Leff, A. F. Rex, Eds., *Maxwell’s Demon* (Adam Hilger, Bristol, 1990).
28. H. C. von Baeyer, *Warmth Disperses and Time Passes* (Random House, New York, 1999).
29. C. Bennett, *Sci. Am.* **257**, 108 (1987).
30. S. Lloyd, *Phys. Rev. A* **39**, 5378 (1989).
31. ———, *Phys. Rev. A* **56**, 3374 (1997).
32. T. Freedmann et al., *Phys. Rev. E* **61**, 4774 (2000).
33. R. Kosloff, E. Geva, J. Gordon, *J. Appl. Phys.* **87**, 8093 (2000).
34. S. Haroche, D. Kleppner, *Phys. Today* **42** (no. 1), 24 (1989).
35. P. R. Berman, Ed., *Cavity Quantum Electrodynamics* (Academic Press, Boston, 1994), p. 57.
36. P. Filipowicz, J. Javanainen, P. Meystre, *J. Opt. Soc. Am. B* **3**, 906 (1986).
37. K. An, J. J. Childs, R. R. Desari, M. S. Feld, *Phys. Rev. Lett.* **73**, 3375 (1994).
38. M.O.S. wishes to thank N. Ramsey for many stimulating and helpful discussions. This paper is an outgrowth of QHE discussions with D. Kleppner, F. Narducci, T. Opatrny, and N. Ramsey at the TAMU-ONR 2001 workshop. Useful conversations on the subject of radiation thermodynamics with G. Baym, P. Martin, P. Meystre, and W. Phillips are gratefully acknowledged, as are helpful discussions on the present manuscript with K. Annamalai, K. Chapin, R. Curl, D. Depatie, B.-G. Englert, E. Fry, R. Hulet, C. Joachain, K. Kapale, V. Kocharovskiy, S. Lloyd, A. Muthukrishnan, T. Opatrny, M. Pilloff, Y. Rostovtsev, Z. Sariyanni, and G. Sussmann. We thank R. Haden, the Texas Engineering Experiment Station, the Office of Naval Research, the DARPA-QUIST program, and the Welch Foundation for supporting this research.

1 October 2002; accepted 16 December 2002  
 Published online 2 January 2003;  
 10.1126/science.1078955  
 Include this information when citing this paper.

## Au<sub>20</sub>: A Tetrahedral Cluster

Jun Li,<sup>1</sup> Xi Li,<sup>1,2</sup> Hua-Jin Zhai,<sup>1,2</sup> Lai-Sheng Wang<sup>1,2\*</sup>

Photoelectron spectroscopy revealed that a 20-atom gold cluster has an extremely large energy gap, which is even greater than that of C<sub>60</sub>, and an electron affinity comparable with that of C<sub>60</sub>. This observation suggests that the Au<sub>20</sub> cluster should be highly stable and chemically inert. Using relativistic density functional calculations, we found that Au<sub>20</sub> possesses a tetrahedral structure, which is a fragment of the face-centered cubic lattice of bulk gold with a small structural relaxation. Au<sub>20</sub> is thus a unique molecule with atomic packing similar to that of bulk gold but with very different properties.

Small clusters often have different physical and chemical properties than their bulk counterparts. Materials assembled from finite-sized clusters have been intensively sought ever since the discovery of C<sub>60</sub> (1). One of the criteria for a cluster to be used as a potential building block for cluster-assembled materials is its chemical

stability relative to other reagents and to other clusters of the same material. A closed electron configuration with a large energy gap between the highest occupied molecular orbital (HOMO) and the lowest unoccupied molecular orbital (LUMO) is a prerequisite for the chemical stability of a cluster. Besides its high sym-

metry, the large HOMO-LUMO gap of  $C_{60}$  is responsible for its chemical inertness and its ability to assemble into molecular crystals (2).

Gold is undoubtedly an important material, and small clusters of gold have also attracted great attention. Although gold colloids have been used for centuries to stain glass (3), more recently it has been shown that gold clusters have unusual catalytic properties for selective oxidation of CO (4–7), are oxidation-resistant (8), enable selective binding of DNA (9), and have potential applications in nanoelectronics (10–16). Small Au cluster cations possess planar structures up to  $Au_7^+$  (17), whereas Au cluster anions are planar up to at least  $Au_{12}^-$  (18, 19). We have probed the electronic and geometrical structures of small Au clusters using anion photoelectron spectroscopy (PES) and computer simulation. The improved instrumental resolution (20) and the ability to produce cold clusters (21) enabled us to obtain considerably more detailed electronic structure information than was previously possible (22). We found that 20-atom gold clusters exhibit a HOMO-LUMO gap even greater than that of  $C_{60}$ . Relativistic density functional calculations predict that  $Au_{20}$  possesses a tetrahedral geometry, similar to that of a fragment of the bulk face-centered cubic (fcc) crystal of gold.

Details of our PES apparatus have been described elsewhere (20, 23). Small  $Au_n^-$  clusters were produced by means of laser vaporization of a pure gold target with a helium carrier gas and were mass-analyzed with time-of-flight mass spectrometry. Pure  $Au_{20}^-$  clusters were selected and decelerated before photodetachment by a pulsed laser beam. Figure 1 shows the PES spectra of  $Au_{20}^-$  at three photon energies. The 193-nm spectrum of  $Au_{20}^-$  (Fig. 1C) displays a weak peak around 2.7 eV (labeled X), followed by a large energy gap and more discrete transitions at higher binding energies (A, B, C, . . .). This spectral pattern suggests that neutral  $Au_{20}$  is a closed-shell molecule with a large HOMO-LUMO gap.

The extra electron that enters the LUMO of  $Au_{20}$  is removed upon photodetachment of the anion, yielding the neutral ground state (X in Fig. 1). The feature A corresponds to the lowest triplet excited state of the neutral. Thus, the A-X separation, measured to be 1.77 eV (Fig. 1B), represents the excitation energy of the first triplet excited state of neutral  $Au_{20}$  but is also an approximate experimental measure of the HOMO-LUMO gap. This energy

gap in  $Au_{20}$  is very large, about 0.2 eV greater than that in  $C_{60}$  (1.57 eV) (24) (Fig. 2). However, electron signals were observed in the HOMO-LUMO gap region in the 266-nm spectrum (Fig. 1B), owing to autodetachment, as a result of a photoexcited  $Au_{20}^{*-}$  upon absorption of a 266-nm photon. Similar autodetachment signals were also observed previously in  $C_{60}^-$  (Fig. 2A) (24). The 355-nm spectrum of  $Au_{20}^-$  revealed a very sharp peak at the ground state transition (autodetachment signals were also observed at this detachment energy), suggesting that there is very little geometry change between the ground states of  $Au_{20}^-$  and neutral  $Au_{20}$ . This is different from  $C_{60}^-$ , whose PES spectra exhibit vibrational features due to structural distortions of the anion ground state (25). The 355-nm spectrum yielded a vertical detachment energy of  $2.751 \pm 0.010$  eV and an adiabatic detachment energy of  $2.745 \pm 0.015$  eV for  $Au_{20}^-$ . The latter is the electron affinity (EA) of  $Au_{20}$ ; a measure of how tightly the cluster can bind an electron. The EA of  $Au_{20}$  is higher than that of  $C_{60}$  (2.689 eV) (24), so  $Au_{20}$  is even more electronegative than  $C_{60}$ .

According to the electron shell model (26),  $Au_{20}$  with 20 valence electrons should represent a major shell closing. What is sur-

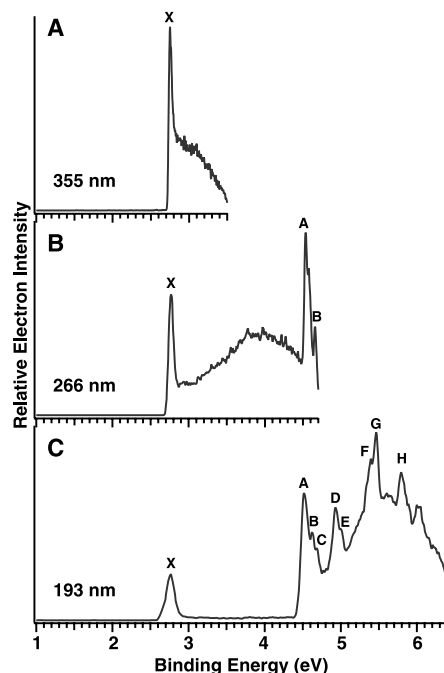


**Fig. 1.** Photoelectron spectra of  $Au_{20}^-$ . (A) At 355 nm (3.496 eV). (B) At 266 nm (4.661 eV). (C) At 193 nm (6.424 eV). The 355- and 266-nm photons were from a Nd-yttrium-aluminum-garnet laser, and the 193-nm photons were from an ArF excimer laser. Photoelectrons were analyzed with a magnetic bottle-type photoelectron spectrometer and calibrated using the known spectrum of  $Rh^-$ . The electron kinetic energy resolution was about 2.5%; that is,  $\sim 25$  meV for 1-eV electrons.

prising is the magnitude of the HOMO-LUMO gap. With the exception of  $Au_2$  and  $Au_6$ , the HOMO-LUMO gap observed for  $Au_{20}$  is the largest among all known coinage-metal clusters (22). It is also larger than that observed in the recently discovered 18-electron icosahedral  $W@Au_{12}$  cluster (27, 28).

The large HOMO-LUMO gap suggests that  $Au_{20}$  should be very inert and may possess a highly symmetric geometry. To elucidate its structure and bonding, we carried out an extensive structural search for neutral and negatively charged  $Au_{20}$ , using relativistic density functional calculations (29–33). We started from the highest symmetry possible [the Platonic dodecahedron with icosahedral ( $I_h$ ) symmetry and octahedron with octahedral ( $O_h$ ) symmetry] to their various important subgroups, as well as the ring and bowl structures known for  $C_{20}$  (34) (Table 1 and Fig. 3). We also tested a capped decahedron ( $C_{2v}$ ) structure (Fig. 3C) and an amorphous ( $C_1$ ) structure (Fig. 3B), which were found as “global” minima in previous calculations (35, 36). The  $I_h$  and  $O_h$   $Au_{20}$  structures are open-shell structures and would be subject to Jahn-

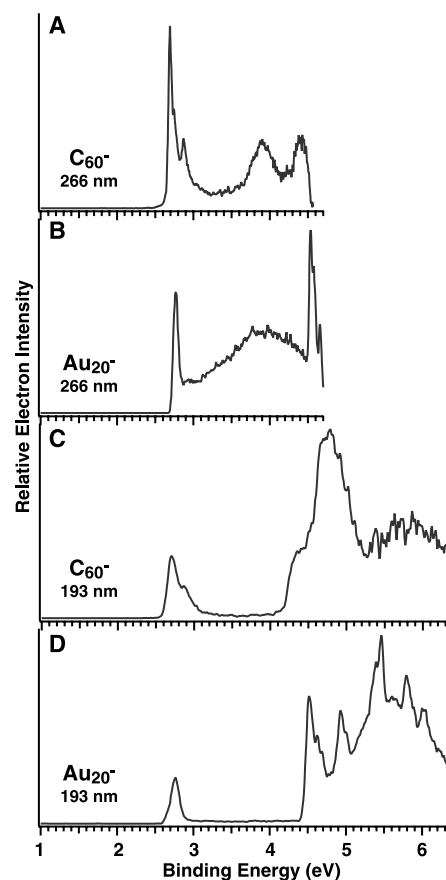


**Fig. 2.** Comparison of the photoelectron spectra of  $Au_{20}^-$  with those of  $C_{60}^-$ . (A) The 266-nm spectrum of  $C_{60}^-$ . “AD” stands for autodetachment signals. (B) The 266-nm spectrum of  $Au_{20}^-$ . (C) The 193-nm spectrum of  $C_{60}^-$ . (D) The 193-nm spectrum of  $Au_{20}^-$ .  $C_{60}^-$  data are from (24).

<sup>1</sup>W. R. Wiley Environmental Molecular Sciences Laboratory, Pacific Northwest National Laboratory, Post Office Box 999, Richland, WA 99352, USA. <sup>2</sup>Department of Physics, Washington State University, 2710 University Drive, Richland, WA 99352, USA.

\*To whom correspondence should be addressed. E-mail: ls.wang@pnl.gov.

## REPORTS

**Table 1.** Optimized molecular structures, point group symmetries, electronic configurations, HOMO-LUMO energy gaps ( $\Delta E_{\text{HL}}$ ), relative scalar-relativistic energies ( $E_{\text{SR}}$ ), and EAs of  $\text{Au}_{20}$ . The relative scalar-relativistic energies of the optimized anions are also listed [ $E_{\text{SR}}(\text{anion})$ ]. All energies are in eV. The total energies of the various isomers of  $\text{Au}_{20}$  and  $\text{Au}_{20}^-$  are relative to those of the neutral tetrahedral  $\text{Au}_{20}$ .

Structure	Group	Configuration	$\Delta E_{\text{HL}}$	$E_{\text{SR}}$	$E_{\text{SR}}(\text{anion})$	EA
Tetrahedral pyramid	$T_d$	$(t_2)^6(e)^4(t_2)^0$	1.818	0	-2.612	2.612
No symmetry	$C_1$	$(a)^2(a)^2(a)^0$	0.495	1.395	-1.767	3.162
Capped decahedron	$C_{2v}$	$(a_1)^2(a_1)^2(b_2)^0$	0.204	1.779	-1.616	3.395
Planar	$C_{2h}$	$(a_g)^2(b_u)^2(b_u)^0$	0.689	2.063	-1.636	3.699
Octahedron	$O_h$	$(a_{1g})^2(e_g)^2(t_{1u})^0$	0	2.509	-0.484	2.993
String-bag cage	$D_{2h}$	$(a_{1g})^2(b_{2u})^2(b_{3g})^0$	0.170	2.898	-0.729	3.627
Dodecahedron	$I_h$	$(h_g)^{10}(g_u)^2(t_{2u})^0$	0	8.466	4.842	3.624
Bowl	$C_{3v}$	$(e_2)^4(e_1)^4(e_1)^0$	0.087	10.504	6.176	4.328
Ring	$D_{5h}$	$(e_1')^4(a_2')^2(a_1')^0$	0.737	11.520	7.249	4.271
Chain	$C_{\infty v}$	$(\sigma)^2(\pi)^4(\pi)^4(\sigma)^0$	0.003	17.625	12.101	5.524

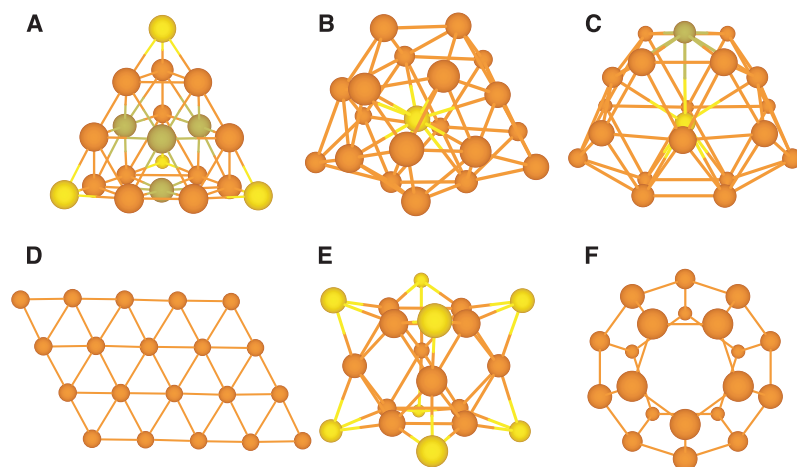


**Fig. 3.** Selected optimized  $\text{Au}_{20}$  structures. (A) Tetrahedral structure ( $T_d$ ). (B) Amorphous structure ( $C_1$ ). (C) Capped decahedron ( $C_{2v}$ ). (D) Planar structure ( $C_{2h}$ ). (E) Octahedral structure ( $O_h$ ). (F) Dodecahedral structure ( $I_h$ ).

Teller instability; a string-bag-like cage, a bowl, and a ring structure are closed-shell but are highly unstable, with small HOMO-LUMO gaps (Table 1). Because smaller  $\text{Au}_n^-$  ( $n < 13$  atoms) clusters prefer planar geometries (18, 19), we also calculated a planar  $\text{Au}_{20}$  structure (Fig. 3D), as well as a linear  $\text{Au}_{20}$  chain, which has recently been formed on a NiAl surface and studied with scanning tunneling microscopy (STM) (37). Although less stable than the tetrahedral structure, the planar structure was found to be more stable than any other isomers except the amorphous cluster (Fig. 3B) and the capped decahedron (Fig. 3C). The linear chain is highly unstable, with almost no HOMO-LUMO gap, which is consistent with its metallic behavior observed by STM (37). The most stable structure we found was the ideal tetrahedral ( $T_d$ ) structure, which is more stable than the previously suggested "global minima"  $C_1$  and  $C_{2v}$  structures by 1.4 and 1.8 eV, respectively. The  $T_d$   $\text{Au}_{20}$  structure is closed-shell, with a HOMO-LUMO gap of 1.8 eV, in excellent agreement with the experiment. The

Au-Au distances (0.268, 0.271, 0.283, 0.297, and 0.312 nm) in the calculated  $T_d$   $\text{Au}_{20}$  structure are close to those in bulk gold (0.288 nm), yielding a tetrahedral edge around 1 nm. Frequency calculations for the  $T_d$   $\text{Au}_{20}$  structure confirmed that it is a minimum on the potential energy surface.

To facilitate comparison with experimental results, we also optimized the geometries of the anions for all the isomers (Table 1). Consistent with the experiment, very little structural change was observed upon electron addition to  $T_d$   $\text{Au}_{20}$ : The Jahn-Teller distortion energy ( $\sim 0.02$  to  $0.04$  eV for distortion to the  $D_{2d}$  and  $C_{3v}$  symmetries) is much smaller than the spin-orbit coupling energy (0.16 eV), so that the geometry distortion is quenched. The total energy difference between the anion and the neutral defines the theoretical EA. The calculated EA for  $T_d$   $\text{Au}_{20}$  is 2.61 eV. However, when spin-orbit coupling is included, we obtain a theoretical EA of 2.741 eV, which is in excellent agreement with the experimental value of 2.745 eV, whereas the calculated EAs for all other

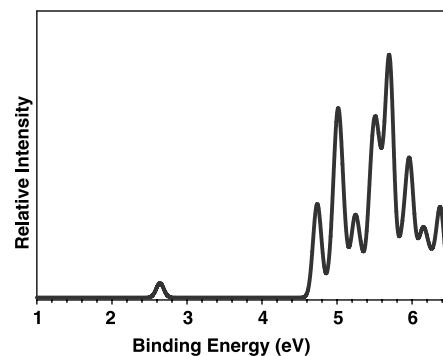


**Fig. 4.** The simulated photoelectron spectrum of  $\text{Au}_{20}^-$ . The simulated spectrum was constructed by fitting the distribution of the calculated detachment transition energies with unit-area Gaussian functions of 0.05 eV at full width at half maximum.

structures deviate considerably from the experimental measurement (Table 1).

Because the  $X-A$  gap (Fig. 1) represents the excitation energy of the lowest triplet excited state, we also calculated this quantity for  $T_d$   $\text{Au}_{20}$ . The calculated excitation energy for the lowest triplet state ( $^3A_1$ ) is 1.777 eV, in close agreement with the experimentally determined value of 1.77 eV. The excellent agreement between the calculated EA and excitation energy and the experimental measurements can probably be attributed to the fact that very little change in geometry exists between the anion ground state and the neutral ground and excited states, and it confirms unequivocally that  $\text{Au}_{20}$  possesses a tetrahedral structure. Further confirmation of the  $T_d$  structure is provided by the theoretical detachment spectrum (Fig. 4), which shows that major PES features are all well reproduced in the simulated spectrum for  $T_d$   $\text{Au}_{20}^-$  (38).

Tetrahedral  $\text{Au}_{20}$  is a small piece of bulk gold with a small relaxation. Each of the four faces represents a (111) surface of fcc gold. It has a very high surface area (all the atoms are on the cluster surface) and a large fraction of corner sites with low coordination. The three different kinds of atoms in the  $T_d$  structure, 4 at the apexes, 4 at the center of each face, and 12 along the edges (Fig. 3A), have different coordination environments and may provide ideal surface sites to bind different molecules for catalysis (such as  $\text{CO}$ ,  $\text{O}_2$ , and  $\text{CO}_2$ ) (39). The large HOMO-LUMO gap of  $\text{Au}_{20}$  suggests that it is a highly inert and stable molecule and may possess novel chemical and physical properties; its unique tetrahedral structure makes  $\text{Au}_{20}$  an ideal model for gold surfaces.

### References and Notes

- H. W. Kroto, J. R. Heath, S. C. O'Brien, R. F. Curl, R. E. Smalley, *Nature* **318**, 162 (1985).
- W. Krätschmer, L. D. Lamb, K. Fostiropoulos, D. R. Huffman, *Nature* **347**, 354 (1990).
- M. A. Hayat, Ed., *Colloidal Gold: Principles, Methods, and Applications* (Academic Press, New York, 1989).

4. M. Valden, X. Lai, D. W. Goodman, *Science* **281**, 1647 (1998).
5. U. Heiz, W. D. Schneider, *J. Phys. D Appl. Phys.* **33**, R85 (2000).
6. A. Sanchez et al., *J. Phys. Chem. A* **103**, 9573 (1999).
7. N. Lopez, J. K. Nørskov, *J. Am. Chem. Soc.* **124**, 11262 (2002).
8. H.-G. Boyen et al., *Science* **297**, 1533 (2002).
9. R. Elghanian, J. J. Storchhoff, R. C. Mucic, R. L. Letsinger, C. A. Mirkin, *Science* **277**, 1078 (1997).
10. S. Chen et al., *Science* **280**, 2098 (1998).
11. R. L. Whetten et al., *Acc. Chem. Res.* **32**, 397 (1999).
12. A. C. Templeton, W. P. Wuefing, R. W. Murray, *Acc. Chem. Res.* **33**, 27 (2000).
13. W. D. Luedtke, U. Landman, *J. Phys. Chem.* **100**, 13323 (1996).
14. O. D. Häberlen, S. C. Chung, M. Stener, N. Rösch, *J. Chem. Phys.* **106**, 5189 (1997).
15. I. L. Garzón et al., *Phys. Rev. Lett.* **81**, 1600 (1998).
16. V. Bonacic-Koutecky et al., *J. Chem. Phys.* **117**, 3120 (2002).
17. S. Gilb, P. Weis, F. Furche, R. Ahlrichs, M. M. Kappes, *J. Chem. Phys.* **116**, 4094 (2002).
18. H. Häkkinen, M. Moseler, U. Landman, *Phys. Rev. Lett.* **89**, 033401 (2002).
19. F. Furche et al., *J. Chem. Phys.* **117**, 6982 (2002).
20. L. S. Wang, C. F. Ding, X. B. Wang, S. E. Barlow, *Rev. Sci. Instrum.* **70**, 1957 (1999).
21. L. S. Wang, X. Li, in *Cluster and Nanostructure Interfaces*, P. Jena, S. N. Khanna, B. K. Rao, Eds. (World Scientific, Singapore, 2000), pp. 293–300.
22. K. J. Tarlor, C. L. Pettiette-Hall, O. Cheshnovsky, R. E. Smalley, *J. Chem. Phys.* **96**, 3319 (1992).
23. L. S. Wang, H. S. Cheng, J. Fan, *J. Chem. Phys.* **102**, 9480 (1995).
24. X. B. Wang, C. F. Ding, L. S. Wang, *J. Chem. Phys.* **110**, 8217 (1999).
25. O. Gunnarsson et al., *Phys. Rev. Lett.* **74**, 1875 (1995).
26. W. A. de Heer, *Rev. Mod. Phys.* **65**, 611 (1993).
27. P. Pyykkö, N. Runeberg, *Angew. Chem. Int. Ed.* **41**, 2174 (2002).
28. X. Li, B. Kiran, J. Li, H. J. Zhai, L. S. Wang, *Angew. Chem. Int. Ed.* **41**, 4786 (2002).
29. Relativistic density functional calculations on Au<sub>20</sub> and its anion were performed at the level of a generalized gradient approach using a Perdew-Wang exchange-correlation functional (30). The zero-order regular approximation Hamiltonian was used to account for the scalar (mass velocity and Darwin) and spin-orbit relativistic effects (31). The standard Slater-type orbital basis sets with quality of triple-zeta plus *p*- and *f*-polarization functions (TZ2P) were used for the valence orbitals of the Au atoms, with frozen core approximation to the [1s<sup>2</sup> 2s<sup>2</sup> 2p<sup>6</sup> 3s<sup>2</sup> 3p<sup>6</sup> 3d<sup>10</sup>] core. The vertical detachment energies of the anions were calculated via the self-consistent field energy difference between the neutral and anion ground states and the excitation energies of the neutral state calculated by the time-dependent density functional theory method (32). All the calculations were accomplished with the Amsterdam Density Functional (ADF 2002) program (33). We found that these theoretical methods are suitable for smaller gold clusters, as well as for gold clusters doped with an impurity atom (28).
30. J. P. Perdew, Y. Wang, *Phys. Rev. B* **45**, 13244 (1992).
31. E. van Lenthe, E. J. Baerends, J. G. Snijders, *J. Chem. Phys.* **99**, 4597 (1993).
32. S. J. A. van Gisbergen, J. G. Snijders, E. J. Baerends, *Comput. Phys. Commun.* **118**, 119 (1999).
33. ADF 2002, SCM, Theoretical Chemistry, Vrije Universiteit, Amsterdam, Netherlands ([www.scm.com](http://www.scm.com)).
34. H. Prinzbach et al., *Nature* **407**, 60 (2000).
35. N. T. Wilson, R. L. Johnston, *Eur. Phys. J. D* **12**, 161 (2000).
36. J. Wang, G. Wang, J. Zhao, *Phys. Rev. B* **66**, 354181 (2002).
37. N. Niluis, T. M. Wallis, W. Ho, *Science* **297**, 1853 (2002).
38. The calculations show that the A, B, and C peaks in the PES spectra (Fig. 1) correspond to the triplet and singlet states formed by electron detachment from the HOMO (16e) and HOMO-1 (29t<sub>2</sub>), whereas the D and E peaks are due to transitions from HOMO-2

(18t<sub>1</sub>). See the supporting online material (fig. S1) for the molecular orbital energy-level diagram of T<sub>d</sub> Au<sub>20</sub><sup>-</sup>.

39. Preliminary calculations on four CO molecules adsorbed on the apex and face-center sites reveal a HOMO-LUMO gap of 1.43 and 1.50 eV for the Au<sub>20</sub>(CO)<sub>4</sub> clusters and a binding energy of 0.84 and 0.15 eV per CO molecule, respectively. The large HOMO-LUMO gaps in the naked and CO-adsorbed clusters indicate that the T<sub>d</sub> Au<sub>20</sub> is highly chemically inert and will maintain its structural integrity during catalysis.
40. We thank B. Kiran for helpful discussion. This work was supported by NSF (grant CHE-9817811) and performed at the Environmental Molecular Sciences

Laboratory (EMSL), a national scientific user facility sponsored by the U.S. Department of Energy's (DOE's) Office of Biological and Environmental Research and located at Pacific Northwest National Laboratory, operated for DOE by Battelle. All the calculations were performed with supercomputers at the EMSL Molecular Science Computing Facility.

#### Supporting Online Material

[www.sciencemag.org/cgi/content/full/299/5608/864/DC1](http://www.sciencemag.org/cgi/content/full/299/5608/864/DC1)

Fig. S1

Reference

29 October 2002; accepted 7 January 2003

## Carbon Tunneling from a Single Quantum State

Peter S. Zuev,<sup>1</sup> Robert S. Sheridan,<sup>1\*</sup> Titus V. Albu,<sup>2</sup>  
Donald G. Truhlar,<sup>2\*</sup> David A. Hrovat,<sup>3</sup>  
Weston Thatcher Borden<sup>3\*</sup>

We observed ring expansion of 1-methylcyclobutylfluorocarbene at 8 kelvin, a reaction that involves carbon tunneling. The measured rate constants were  $4.0 \times 10^{-6}$  per second in nitrogen and  $4 \times 10^{-5}$  per second in argon. Calculations indicated that at this temperature the reaction proceeds from a single quantum state of the reactant so that the computed rate constant has achieved a temperature-independent limit. According to calculations, the tunneling contribution to the rate is 152 orders of magnitude greater than the contribution from passage over the barrier. We discuss environmental effects of the solid-state inert-gas matrix on the reaction rate.

Quantum mechanical tunneling frequently plays an important role in reactions in which a hydrogen atom (1), proton (2, 3), or hydride ion (3) is transferred. In most organic reactions, motion of carbon is also part of the reaction coordinate, and kinetic isotope effects are consistent with a contribution from carbon motion in some tunneling reactions (4). However, evidence for tunneling in reactions that are dominated by carbon motion is rare.

One reaction in which there is good experimental and theoretical evidence for carbon tunneling is the automerization of 1,3-cyclobutadiene (5–7). In this reaction, the carbons each need to move only about 0.1 Å, resulting in a thin barrier that favors tunneling (5). This reaction has been observed at 25 K in an argon matrix (6), and tunneling still occurs, despite the solid-state environment of the reactant (8).

A few other transformations that involve the making or breaking of C–C σ bonds have

been observed at very low temperatures, where there is unlikely to be thermal energy sufficient to allow molecules to surmount any but the most minuscule barriers to reaction (9–11). The finite rates observed in these reactions suggest that carbon tunneling may be involved. However, the interpretation of these experiments is complicated because in each case, the rate-determining step apparently involves intersystem crossing to an electronic state from which the observed reaction is likely to occur without a barrier.

Tunneling by carbon might play a role in 1,2-shifts in singlet carbenes. The distance between the carbene center and the carbon that migrates to it changes by about 1 Å in these exothermic rearrangements. However, tunneling appears to make only minor contributions to the rates of ring expansions of cyclopropylhalocarbenes in liquid solution at 298 K (12). Nevertheless, rearrangements of cyclobutylhalocarbenes to 1-halocyclopentenes are expected to have lower barriers, because in these reactions there is less hyperconjugative stabilization of the reactants and more relief of ring strain in the products than in the ring expansions of cyclopropylhalocarbenes. Indeed, cyclobutylhalocarbenes are shorter-lived in solution at room temperature than are the corresponding cyclopropylhalocarbenes (13, 14).

Here, we report an experimental and com-

<sup>1</sup>Department of Chemistry 216, University of Nevada, Reno, NV 89557, USA. <sup>2</sup>Department of Chemistry and Supercomputer Institute, University of Minnesota, Minneapolis, MN 55455–0431, USA. <sup>3</sup>Department of Chemistry, Box 351700, University of Washington, Seattle, WA 98195–1700, USA.

\*To whom correspondence should be addressed. E-mail: rss@unr.edu (R.S.S.); truhlar@umn.edu (D.G.T.); borden@chem.washington.edu (W.T.B.)

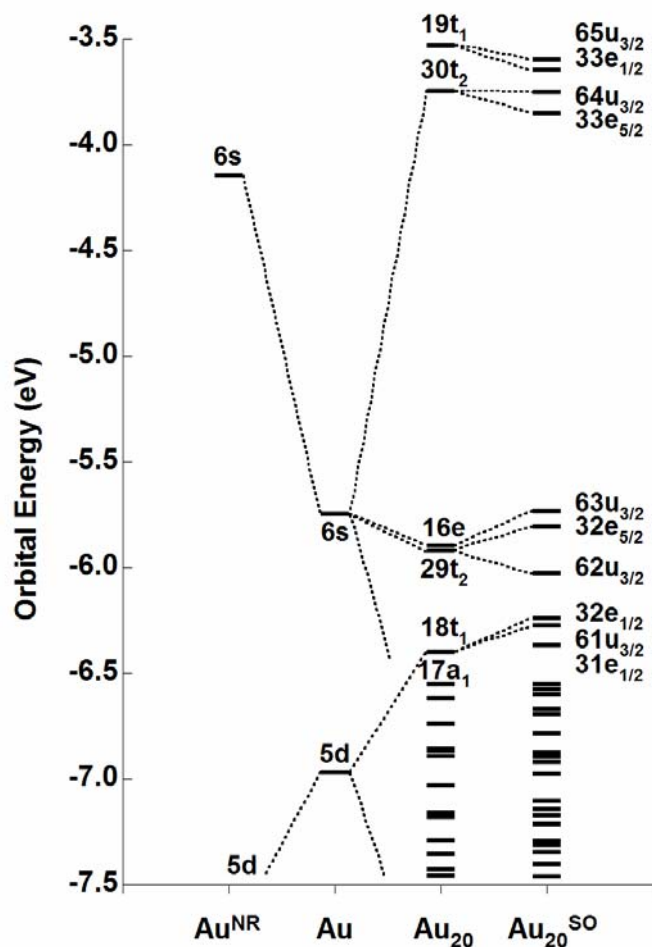


**Fig. S1.** The molecular orbital energy-level diagram of the  $T_d$   $\text{Au}_{20}$  with spin-orbit splitting ( $\text{Au}_{20}^{\text{SO}}$ ). The correlation diagram to the levels of the Au atom is also shown, as well as the spin-orbit effect for Au. NR stands for non-relativistic. The Au 6s orbital is considerably stabilized while the Au 5d orbitals are destabilized due to the scalar relativistic effects (SR). The LUMO of  $\text{Au}_{20}$  is triply degenerate ( $30t_2$ ) and the HOMO is doubly degenerate (16e). The triply degenerate HOMO-1 ( $29t_2$ ) is accidentally near-degenerate to the HOMO. The spin-orbit coupling effects on these frontier orbitals are 0.17 and 0.22 eV for the LUMO and HOMO-1, respectively.

## Reference

S1. P. Pyykkö, *Chem. Rev.* **88**, 563 (1988).

